The Astrophysical Journal, 988:153 (16pp), 2025 August 1 https://doi.org/10.3847/1538-4357/ade14c

A Multi-wavelength Characterization of the 2023 Outburst of MAXI J1807+132: Manifestations of Disk Instability and Jet Emission

Sandeep K. Rout[1,2], M. Cristina Baglio[3], Andrew K. Hughes[4,5], David M. Russell[1,2], D. M. Bramich[1,2], Payaswini Saikia[1,2], Kevin Alabarta[1,2], Montserrat Armas Padilla[6,7], Sergio Campana[3], Stefano Covino[3,8], Paolo D'Avanzo[3], Rob Fender[4], Paolo Goldoni[9], Jeroen Homan[10], Fraser Lewis[11,12], Nicola Masetti[13,14], Sara Motta[3], Teo Muñoz-Darias[6,7], Alessandro Papitto[15], Thomas D. Russell[16], Gregory Sivakoff[5], and Jakob van den Eijnden[17]

[1] New York University Abu Dhabi, PO Box 129188, Abu Dhabi, UAE; sandeep.rout@nyu.edu
[2] Center for Astrophysics and Space Science (CASS), New York University Abu Dhabi, PO Box 129188, Abu Dhabi, UAE
[3] INAF—Osservatorio Astronomico di Brera, Via Bianchi 46, I-23807 Merate (LC), Italy
[4] Department of Physics, University of Oxford, Denys Wilkinson Building, Keble Road, Oxford OX1 3RH, UK
[5] Department of Physics, University of Alberta, Edmonton, T6G 2E1, Canada
[6] Instituto de Astrofísica de Canarias (IAC), Vía Láctea s/n, La Laguna E-38205, S/C de Tenerife, Spain
[7] Departamento de Astrofísica, Universidad de La Laguna, La Laguna E-38205, S/C de Tenerife, Spain
[8] Como Lake Centre for AstroPhysics (CLAP), DiSAT, Universitá dell'Insubria, via Valleggio 11, 22100 Como, Italy
[9] Université Paris Cité, CNRS, CEA, Astroparticule et Cosmologie, F-75013 Paris, France
[10] Eureka Scientific, Inc., 2452 Delmer Street, Oakland, CA 94602, USA
[11] Faulkes Telescope Project, School of Physics and Astronomy, Cardiff University, The Parade, Cardiff, CF24 3AA Wales, UK
[12] The Schools' Observatory, Astrophysics Research Institute, Liverpool John Moores University, 146 Brownlow Hill, Liverpool L3 5RF, UK
[13] INAF—Osservatorio di Astrofisica e Scienza dello Spazio, Via Piero Gobetti 101, I-40129 Bologna, Italy
[14] Universidad Andrés Bello, Av. Fernández Concha 700, Las Condes, Santiago, Chile
[15] INAF Osservatorio Astronomico di Roma, Via Frascati 33, I-00078 Monte Porzio Catone (RM), Italy
[16] INAF, Istituto di Astrofisica Spaziale e Fisica Cosmica, Via U. La Malfa 153, I-90146 Palermo, Italy
[17] Anton Pannekoek Institute for Astronomy, Universiteit van Amsterdam, Science Park 904, 1098, XH, Amsterdam, The Netherlands

Received 2025 March 20; revised 2025 May 28; accepted 2025 June 3; published 2025 July 21

Abstract

Several phenomenological aspects of low-luminosity neutron star transients, such as atolls, remain poorly understood. One such source, MAXI J1807+132, entered its latest outburst in 2023 July. To thoroughly characterize this outburst, we conducted an extensive observational campaign spanning radio to X-ray wavelengths. Here we present the results of this campaign, which covered the period from before the outburst to the return to quiescence. We detected a delay between the X-ray and optical rise times, which is consistent with the predictions of the disk instability model with a truncated disk. The color evolution and optical/X-ray correlations, along with infrared and radio detections, support the presence of jet synchrotron emission during the gradual decay phase following the peak. We also report for the first time in an X-ray binary a near-orthogonal rotation of the optical polarization just before a small flare, after which the jet is thought to be quenched. The main outburst is followed by several high-amplitude, rapid reflares in the optical, ultraviolet, and X-ray bands, the origin of which remains difficult to constrain.

Unified Astronomy Thesaurus concepts: Low-mass x-ray binary stars (939); Neutron stars (1108); Jets (870); Accretion (14)

1. Introduction

Low-mass X-ray binaries (LMXBs) are transient systems in which a compact object, that is, a black hole (BH) or neutron star (NS), accretes matter from a low-mass star via Roche-lobe overflow. The outburst and quiescence cycle in LMXBs are typically explained by the disk-instability model (DIM; see G. Dubus et al. 2001; J.-P. Lasota 2001 for reviews). Although the DIM was originally developed for dwarf novae (J. Smak 1971), it can also be applied to NS and BH LMXBs due to their morphological similarities and the similarities in the rapid rise and exponential decay behavior observed in both types of system (J. van Paradijs & F. Verbunt 1984; J. van Paradijs 1996). To explain the typical phenomenology of LMXBs, several modifications to the DIM have been proposed over the years. Notable modifications have been the inclusion of irradiation effects on the outer disk and companion star, the impact of outflows such as winds and jets on the disk structure, inner disk truncation, and fluctuations in the mass transfer rate (e.g., J. M. Hameury 2020).

The accretion process is often accompanied by the ejection of matter from the system in the form of winds and jets (e.g., R. Fender & E. Gallo 2014; R. Fender & T. Muñoz-Darias 2016; J. Homan et al. 2016). These outflows play a crucial role in the outward transfer of angular momentum and in enriching the surrounding medium with stellar material. Jets often appear as relativistic outflows along the spin axis of the compact object, which are at times found to be misaligned with the orbital plane and undergo precession. The strong magnetic fields that channel these outflows give rise to synchrotron emission, which typically follows a broken power-law spectrum (e.g., R. D. Blandford & A. Königl 1979; H. Falcke et al. 2004). The frequency at which the break occurs, which typically falls in the mid-infrared to optical frequency range, is

Table 1
Summary of All Observations Used in This Work

Bands	Instruments	Energy/Wavelength	MJD	No. of Observations
X-ray	NICER/XTI	0.5–10 keV	60132–60161	38
	Swift/XRT	0.7–10 keV	60137–60238	23
Ultraviolet	Swift/UVOT	$W2$ (1928 Å), $M2$ (2246 Å), $W1$ (2600 Å)	60137–60231	16
Optical	Swift/UVOT	U (3465 Å), V (4392 Å)	60137–60228	18
	Faukes, LCO	g' (4770 Å), r' (6215 Å), i' (7545 Å), z_s (8700 Å)	59326–60239	241
	VLT/FORS2	B (440 nm), V (557 nm), R (655 nm), I (768 nm)	60142, 60143, 60149	3
Infrared	REM	H (1.64 μm)	60138–60184	7
Radio	VLA	A-band (1.5 GHz), C-band (6 GHz)	60202–60226	7
	MeerKAT	L-band (1.28 GHz)	60132–60231	15

Note. The last column contains the total number of observations in all the filters/bands mentioned in the third column.

an important observable for determining the total energy output of the jet (e.g., T. D. Russell et al. 2014). However, measuring the break frequency is not straightforward, as it requires simultaneous broadband coverage spanning several orders of magnitude in frequency (e.g., D. M. Russell et al. 2013a).

In BH LMXBs, jet emission is strongly linked to the spectral state of the source. Compact jets are typically detected in the low-hard state, while ballistic jets are observed during the transition from the hard-intermediate to the soft-intermediate states (R. P. Fender et al. 2004, 2009; F. Carotenuto et al. 2021). NS systems are subclassified into Z and atoll sources based on their position on the X-ray color–color diagram (G. Hasinger & M. van der Klis 1989). They mainly differ in their luminosities, with the former being brighter than the latter. In Z sources, jets are brightest in the horizontal branch and fade along the normal and flaring branches (W. Penninx et al. 1988; R. M. Hjellming et al. 1990; S. Migliari & R. P. Fender 2006). Similarly, in atoll sources, jets are typically brighter in the hard island branches and fainter in the banana branches. In general, jets are brighter in the low accretion rate, radiatively inefficient phases and fainter in high accretion rate states. However, unlike their BH counterparts, the association between jet brightness and spectral states is not as strict in NS sources. For example, an increase in the radio flux was detected when the Z source GX 17 + 2 moved from the horizontal to the normal branch (J. Tan et al. 1992). Similarly, S. Migliari et al. (2004) detected radio emission in the soft banana branches of the atoll sources 4U 1820–30 and Ser X-1 (see also T. D. Russell et al. 2021, for a detailed discussion on 4U 1820−30). Furthermore, the jets in the NS systems are approximately 22 times fainter than the BH jets, making their study more challenging (e.g., R. P. Fender & E. Kuulkers 2001; D. M. Russell et al. 2007; V. Tudor et al. 2017; E. Gallo et al. 2018). Even the radio/X-ray correlation slopes of Aql X-1, a well-studied atoll source, are complex and debated (e.g., V. Tudose et al. 2009; N. V. Gusinskaia et al. 2020; S. Fijma et al. 2023). Although the radio luminosity of the NS jets is not fully understood, they are generally still correlated with the X-ray emission to some extent (including in the source that switches between Z and atoll states, XTE J1701–462; K. V. S. Gasealahwe et al. 2024).

With the aim of expanding our understanding of the accretion-ejection paradigm in NS LMXBs, we conducted an extensive multiwavelength observing campaign on the atoll source MAXI J1807+132 during its latest outburst in 2023 July. MAXI J1807+132 had undergone two previous outbursts in 2017 and 2019, during which its NS nature was confirmed by the detection of type I thermonuclear bursts (M. Shidatsu et al. 2017; F. Jiménez-Ibarra et al. 2019; A. C. Albayati et al. 2021). We reported the X-ray properties of the source with data from the Neutron Star Interior Composition Explorer (NICER) in a separate paper (S. K. Rout et al. 2025). In this work, we extend the study of the properties of the source to the rest of the wavelengths, that is, ultraviolet (UV) to radio. We rely on the spectral state classification from the X-ray study and also use the 2–10 keV flux values derived from it to study the optical/X-ray correlations. We provide a summary of all the observations used in this work in Table 1. In Section 2 we give details of all the data used in the work along with their reduction. The different diagnostic tools and the main results are detailed in Section 3. In Section 4 we provide an interpretation of the results and compare them with the literature. Finally, in Section 5 we summarize the main results of this work.

2. Observations and Data Reduction

2.1. X-Ray with NICER and Swift

We used data from both Swift and NICER to study the X-ray emission from the source. The analysis of NICER (K. C. Gendreau et al. 2016) data was carried out using `NICERDAS_V011a`. We followed the standard procedures for the extraction of the lightcurves and spectra using the `nicerl3` tools. More details on the reduction are given in S. K. Rout et al. (2025). We used the NICER data to study two things: (1) the delay between the X-ray and optical rise and (2) correlations between the optical and X-ray emission. Specifically for the correlations, we used the unabsorbed flux in the 2–10 keV band from the spectral fits (S. K. Rout et al. 2025). The lightcurves and spectra for the Swift/X-ray Telescope (XRT; D. N. Burrows et al. 2005) were extracted from the XRT data products generator[18] (P. A. Evans et al. 2007; P. A. Evans et al. 2009). This corrects for pile-up effects by selecting an annular extraction region with appropriate inner radius depending on the count rate. Similarly, the effects of grade migration in the piled-up data acquired in the photon-counting mode are mitigated by selecting grade 0–4 events.

---

[18] https://www.swift.ac.uk/user_objects/docs.php

2.2. Optical and Ultraviolet with Swift

Swift started observations of MAXI J1807+132 as soon as the source reached the peak of the 2023 outburst. Both XRT and the Ultraviolet and Optical Telescope (UVOT; P. W. A. Roming et al. 2005) continued the monitoring campaign for about three months after the main outburst and captured several reflaring events. UV photometry was done using the `uvotsource` module in `heasoft-6.32`. A $5''$ circular region centered at the source coordinates was selected for the source photometry, and a $\sim 10''$ circle offset from the source was chosen for the background. Photometric measurements were carried out for the $W1$, $M2$, $W2$, U, and V bands. Some observations were also made in the B band. However, they were acquired near the quiescence level and the source was not significantly detected. Hence, we did not include them in our analysis. Of all of these filters, observations with the V and $W2$ bands were made at simultaneous epochs and with good cadence during the main outburst. Hence, they are used for studying the color evolution and spectral energy distributions (SEDs).

2.3. Optical Photometry with Las Cumbres Observatory

MAXI J1807+132 is a regular target in our LMXB monitoring program with the 2 m Faulkes Telescope and the 1 m telescopes of the Las Cumbres Observatory (LCO) network (F. Lewis et al. 2008). With our fully automated pipeline X-ray Binary New Early Warning System (XB-NEWS; D. M. Russell et al. 2019; A. J. Goodwin et al. 2020), we are able to create near real-time lightcurves of the source in the optical wave bands. As a result of this, we detected the optical rise on 2023 July 2, and a multiwavelength observation campaign was started after that (G. Illiano et al. 2023; P. Saikia et al. 2023a, 2023a).

The optical photometry was carried out using the XB-NEWS pipeline for the SDSS filters z_s, i', r', and g' (K. Alabarta et al. 2025, in preparation). The pipeline scans the LCO archive at regular intervals, and, whenever new observations are available, it downloads the reduced images. Poor-quality images are immediately rejected. For those images that pass the quality control stage, an astrometric solution is derived by comparison to the Gaia DR2 catalog,[19] and then multiaperture photometry (P. B. Stetson 1990) is performed for all detected sources. Flux calibration is done using an enhanced version of the ATLAS-REFCAT2 catalog,[20] which includes other catalogs such as Pan-STARRS DR1,[21] APASS,[22] and so on (J. L. Tonry et al. 2018), by solving for zero-point offsets along the lines of the method given in D. M. Bramich & W. Freudling (2012). When the main target is not formally detected due to faintness, forced photometry is carried out at the target coordinates. Magnitude measurements of the target with uncertainties that exceed 0.25 mag are rejected.

2.4. Optical Polarimetry with the Very Large Telescope

We observed MAXI J1807+132 with the Very Large Telescope (VLT), at Paranal Observatory (Chile), equipped with the Focal Reducer/Low Dispersion Spectrograph 2 (FORS2; I. Appenzeller et al. 1998) instrument in polarimetric mode using the following set of four optical filters: $b\_HIGH + 113$ (B; central wavelength 440 nm), $v\_HIGH + 114$ (V; central wavelength 557 nm), $R\_SPECIAL + 76$ (R; central wavelength 655 nm), and $I\_BESS + 77$ (I; central wavelength 768 nm). Observations were made on three epochs during the outburst: 2023 July 17 (MJD 60142.1), 2023 July 18 (MJD 60143.1), and 2023 July 24 (MJD 60149.0).

A Wollaston prism was inserted into the instrument's optical path, splitting the incoming light into two beams with orthogonal polarization (ordinary and extraordinary). To prevent these beams from overlapping on the CCD, a mask was employed. Additionally, a rotating half-wave plate (HWP) was incorporated, enabling the capture of images at four distinct angles (Φ_i) relative to the telescope position angle: $\Phi_i = 22\overset{\circ}{.}5\ (i - 1)$ with $i = 1, 2, 3, 4$.

With this setup, one image for each of the four HWP angles was captured in each filter for each night employing the following exposure times for each image: 65 s in B, 45 s in V, 40 s in R, and 70 s in I. All images were then processed by subtracting an averaged bias frame and normalizing with a flat field. Aperture photometry was performed using `daophot` (P. B. Stetson 1987), applying a 6 pixel radius aperture (which corresponds to $\sim 0\overset{''}{.}8$).

The linear polarization degree P and polarization angle θ are calculated following the methodology detailed in Section 3.1.1 of M. C. Baglio et al. (2020). These parameters are not corrected for any instrumental contributions to linear polarization. This is justified because unpolarized standard stars routinely observed with FORS2 show that the instrument's polarization has remained stable and very low (below 0.3%, on-axis) across all bands over the past decade. More details on the calculation of the linear polarization and estimation of the posterior probabilities are given in Appendix A.

2.5. Near-infrared with Robotic Eye Mount

We observed MAXI J1807+132 in the H band with the 60 cm Robotic Eye Mount (REM) telescope at La Silla (Chile) from 2023 July 13 (MJD 60138) to 2023 August 28 (MJD 60184), for a total of seven epochs of observations randomly distributed within this date range. For each epoch, three sets of observations were taken, except for MJD 60138 and MJD 60150, where only one set of observations was acquired. Each set consisted of five dithered 30 s integration exposures that were combined for optimal background subtraction. Unfortunately, the signal-to-noise ratio was not always good enough to detect the target, typically due to bad seeing conditions (which reached up to $5''$). In the images where detection was possible, we performed aperture photometry using `daophot` (P. B. Stetson 1987), applying an aperture with radius 2 times the average full width at half-maximum (FWHM) of the flux profiles of the field stars. In the cases where a detection was not possible, we estimated 3σ upper limits to the target flux for those images. Flux calibration was performed against the 2MASS[23] catalog (M. F. Skrutskie et al. 2006).

2.6. Radio with MeerKAT

We observed MAXI J1807+132 with MeerKAT (J. Jonas & Team MeerKAT 2016) as part of the large survey project ThunderKAT (R. Fender et al. 2016). We began our monitoring on 2023 July 7 (MJD 60132), continuing until

---

[19] https://www.cosmos.esa.int/web/gaia/dr2

[20] https://archive.stsci.edu/prepds/atlas-refcat2/

[21] https://panstarrs.stsci.edu

[22] https://www.aavso.org/apass

[23] https://irsa.ipac.caltech.edu/Missions/2mass.html

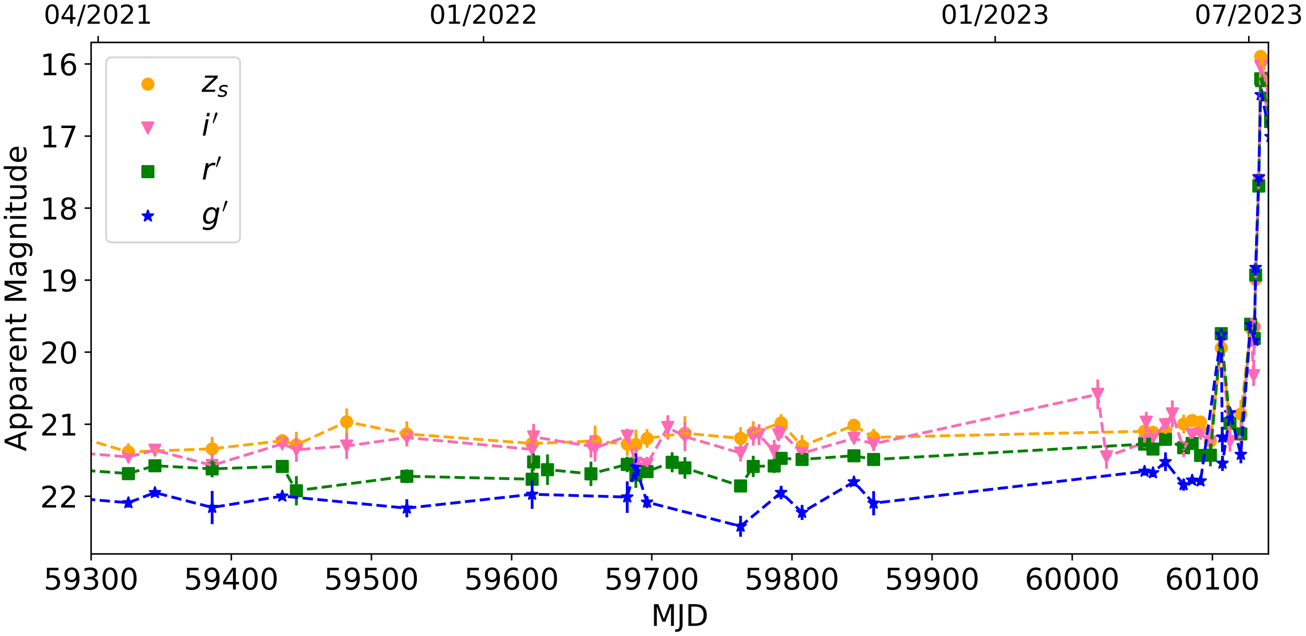

Figure 1. The quiescent optical lightcurve of MAXI J1807+132 since 2021 April, when our regular LCO monitoring started with the SDSS filters, until the beginning of the latest outburst in 2023 July.

2023 October 14 (MJD 60231), totaling 15 observations. Each observation consisted of a single scan of 15 minutes on source flanked by two 2 minute scans of a nearby gain calibrator (J1733−1304). Each epoch also included a 5 minute PKS B1934-638 (J1939−6342) scan for flux and bandpass calibration. All MeerKAT observations used the *L*-band receiver, with a central frequency of 1.28 GHz and a ∼856 MHz bandwidth. We processed the MeerKAT data with the semiautomated pipeline OXKAT (I. Heywood 2020), producing a single image per observing epoch. A comprehensive description of OXKAT is found in I. Heywood et al. (2022). The morphology of the radio emission from MAXI J1807+132 showed temporal variability. To verify its association with the source, we obtained observations with the Very Large Array (VLA). Details on the VLA campaign and its analysis are given in Appendix B.

3. Analysis and Results

3.1. Multiwavelength Lightcurve and X-Ray Delay

The long-term optical lightcurve of MAXI J1807+132 since 2021 April (MJD 59326) until the beginning of the 2023 outburst is shown in Figure 1. The source remained dormant for nearly 20 months until 2022 November (MJD 59894). Following this, there was a four-month gap in our observations. When the observations resumed, the fluxes in the g' and r' bands, and less so in the i' band, were at a slightly elevated level (by ∼0.1–0.2 mag). To determine whether there is a significant difference in the quiescence brightness level before and after the four-month observational gap, we did the following. First, we fit all of the data points between MJD 59300 and 60100 with a constant-brightness model (M1) using χ^2 minimization. Then we fit a second model to the same data, again using χ^2 minimization, where this model has different constant brightnesses for before and after the observational gap (M2). The $\Delta\chi^2$ values between the two models are 58.62, 117.84, 12.78, and 9.00 for the g', r', i', and z_s bands, respectively. Given that there is one more free parameter in M2 compared to M1, we can compare these values with a χ^2 distribution with 1 degree of freedom. In doing so, we find that the $\Delta\chi^2$ values are significant at the 1% level (i.e., they are greater than the threshold of ∼6.62), thereby leading us to reject M1 at this level of significance. LMXBs are sometimes known to undergo a slow rise phase a few years before the onset of the outburst (e.g., D. M. Russell et al. 2018, and references therein). We tested this possibility by fitting the long-term lightcurve with a model consisting of a constant magnitude up to a certain point in time (break point) followed by a linear trend (M3). We iterated the fits for a grid of 8000 break points between MJD 59300 and MJD 60100 and computed the χ^2 for each fit. The best fits for the g' and r' bands occur at the break points of MJD $59763.4^{+27.5}_{-58.8}$ and MJD $59696.6^{+39.8}_{-55.3}$, respectively. However, for the i' and z_s bands, the best-fit break points were found at the lower limit of the time range and therefore could not be constrained. The 90% upper limits of the break points for the i' and z_s bands are MJD 59652.9 and MJD 59743.1, respectively. This model provided a much better fit compared to M1 with $\Delta\chi^2$ between the two models being 60.10, 129.61, 19.67, and 14.13 for the g', r', i', and z_s bands, respectively (again significant at the 1% level). However, M2 is not nested within M3, and both have exactly the same number of free parameters. Hence, we computed the likelihood ratios M3 to M2 for the four filters, which are 2.1, 358.7, 31.3, and 16.3. Hence, the linear rise is significantly favored over a sudden increase in brightness in three out of four filters. We conclude that the source indeed shows a slow rise ∼400 days before the main outburst, with some hints of the redder band fluxes rising earlier than the bluer band fluxes. The rise rates in the g' (0.34 ± 0.07 mag yr^{-1}) and r' (0.30 ± 0.03 mag yr^{-1}) bands are steeper than in the i' (0.11 ± 0.03 mag yr^{-1}) and z_s (0.14 ± 0.03 mag yr^{-1}) bands. We show the fits of M3 to the long-term lightcurves in Appendix C.

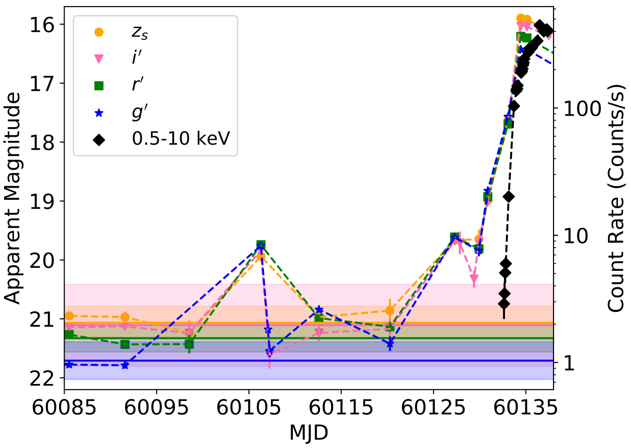

Figure 2. The rise of the 2023 outburst as observed with LCO and NICER. The horizontal shades represent the 3 × rms extent from the mean quiescence levels calculated between MJD 60000 and MJD 60100, for the individual filters.

A brief brightening event was detected on MJD 60106.2, when the magnitudes decreased by more than 1 mag from the quiescence levels in the four LCO filters (Figure 2). This was about 26 days before the first significant X-ray detection with NICER made on MJD 60132.1. Following this event, the fluxes decreased in all the filters to the quiescent levels (Figure 2). On MJD 60127.2, the source brightened up again and continued to rise, although after a small dip in the i' band on MJD 60129.9, until the outburst peak on MJD 60134.4. The optical rise was detected 4.9 days before the first X-ray detection with NICER. The estimation of the delay between the start of the X-ray rise and the start of the optical rise is quite uncertain and depends on the sensitivity of NICER and the gaps in the observations. If the actual X-ray rise started much before the detection (on MJD 60132.1), then the delay would be shorter. On the other hand, if the optical flux started to rise before the second brightening (MJD 60127.2), then the delay would be longer. Considering that the optical epoch previous to the rise was 7 days prior (MJD 60120.2), the actual delay between the start of the optical rise and the start of the X-ray rise could be anywhere between 4 and 12 days. This assumes that the X-ray could start to rise from quiescence by at most one day before its detection, which may not be true.

After reaching the peak on MJD 60134.4, the optical flux gradually decayed until MJD 60150, forming a plateau (Figure 3). On MJD 60147.6 a flare was detected by UVOT in the V and $W2$ filters, about 2.6 days before it was detected in X-rays. This flare was missed by LCO because of gaps in the observations. After the flare, the optical flux declined rapidly until MJD 60157.3, marking the end of the main outburst.

Before reaching the previous quiescence levels, the source started to show several high-amplitude rapid reflares over a period of more than two months. However, because of poor temporal sampling, it is difficult to trace the profiles of the reflares as well as count their exact numbers. Despite this, from the optical, UV, and X-ray lightcurves shown in Figure 3, the presence of at least six reflares can be ascertained. Approximately, they peak around MJDs 60163.4, 60175.4, 60189.2, 60200.8, 60218.9, and 60239.2. With the caveat that the peaks of the fourth and sixth reflares are not well constrained, the duration between each adjacent reflare is ≈12–14 days, which is about twice that observed during the 2017 outburst (F. Jiménez-Ibarra et al. 2019). The emission during the reflares follows a bluer-when-brighter pattern, with the X-rays being the highest amplitude, followed by UV and optical (see Figure 3).

3.2. Spectral Energy Distribution

We studied the SEDs of MAXI J1807+132 to understand the optical emission mechanisms. To derive the SEDs from the apparent magnitudes, we first need the dereddened fluxes. The optical extinction is linearly related to the equivalent hydrogen column density, $N_{\rm H} = (2.62 \pm 0.02) \times 10^{21}\,{\rm cm}^{-2}$, obtained from X-ray measurements (S. K. Rout et al. 2025). The extinction is given by $A_V = \frac{N_{\rm H}}{(2.87 \pm 0.12) \times 10^{21}} = 0.91 \pm 0.04$ mag (D. R. Foight et al. 2016). We used this value of A_V along with the frequency-dependent absorption coefficients from the extinction law of J. A. Cardelli et al. (1989) to deredden the calibrated optical magnitudes of the source. The final optical SEDs were constructed from observations taken in three or more filters within approximately one hour. These SEDs were fit with a power law of the form $F_\nu \propto \nu^\alpha$, where α is the spectral index (Figure 4). The evolution of α during the outburst, along with the multiwavelength lightcurves, is shown in the bottom panel of Figure 3. During quiescence, the optical data exhibit considerable variability, both within individual filters and in the shape of the SEDs. In some cases, the SEDs do not conform to a power law (see Figure 4). The SED may trace the curved peak of the Planck function or be contaminated by emission from the secondary star, making the power law a poor approximation. Nevertheless, it is evident that the overall slope of the SED during quiescence varies over a wide range, between -0.33 ± 0.07 and 0.33 ± 0.23 (1σ). During the optical flare on MJD 60106.2, α increases to 1.19 ± 0.11 and remains there (within errors), even as the flux decreases in the next epoch on MJD 60112.5. On MJD 60120.2, the fluxes in all filters return to near-quiescent levels and the SED becomes flat, with $\alpha = 0.26 \pm 0.23$. MJD 60127.2 marks the rise of the main outburst, characterized by a steepening of the SED ($0.66 < \alpha < 1.26$) until MJD 60134.4, near the peak, when the index suddenly drops to 0.12 ± 0.04. Afterward, α gradually increases in anticorrelation with the flux, reaching 0.57 ± 0.18 on MJD 60157.3, when the main outburst ends. In the first reflare that follows the main outburst, the spectral index tracks the flux, rising to 0.93 ± 0.08 and then dropping to 0.10 ± 0.21. In subsequent reflares, however, the sampling is sparse, making it difficult to trace the evolution of the SED. Generally, around the peak of the reflares, the SED remains steep, with $\alpha \sim 1.0$ (Figure 4). Observations on MJDs 60225.2 and 60235.2 may be exceptions, where $\alpha \sim 0.6$ when the optical fluxes are at quiescent levels. However, these SEDs are based on only two filters (the points marked with black stars in Figure 3 have only two filters and thus no error bars), making it difficult to draw firm conclusions.

3.3. Color Evolution

The color–magnitude diagram (CMD; D. Maitra & C. D. Bailyn 2008), similar to the hardness-intensity diagram in X-rays, is a useful tool for ascertaining state changes and delineating the different emission mechanisms in X-ray transients (D. M. Russell et al. 2011). In Figure 5, we show the CMD with LCO bands (g' vs. $g'-i'$) in the left panel and with UVOT bands ($W2$ vs. $W2 - V$) in the right panel. Swift observations were triggered after the detection of the optical rise, so we have data from the outburst peak until the end of

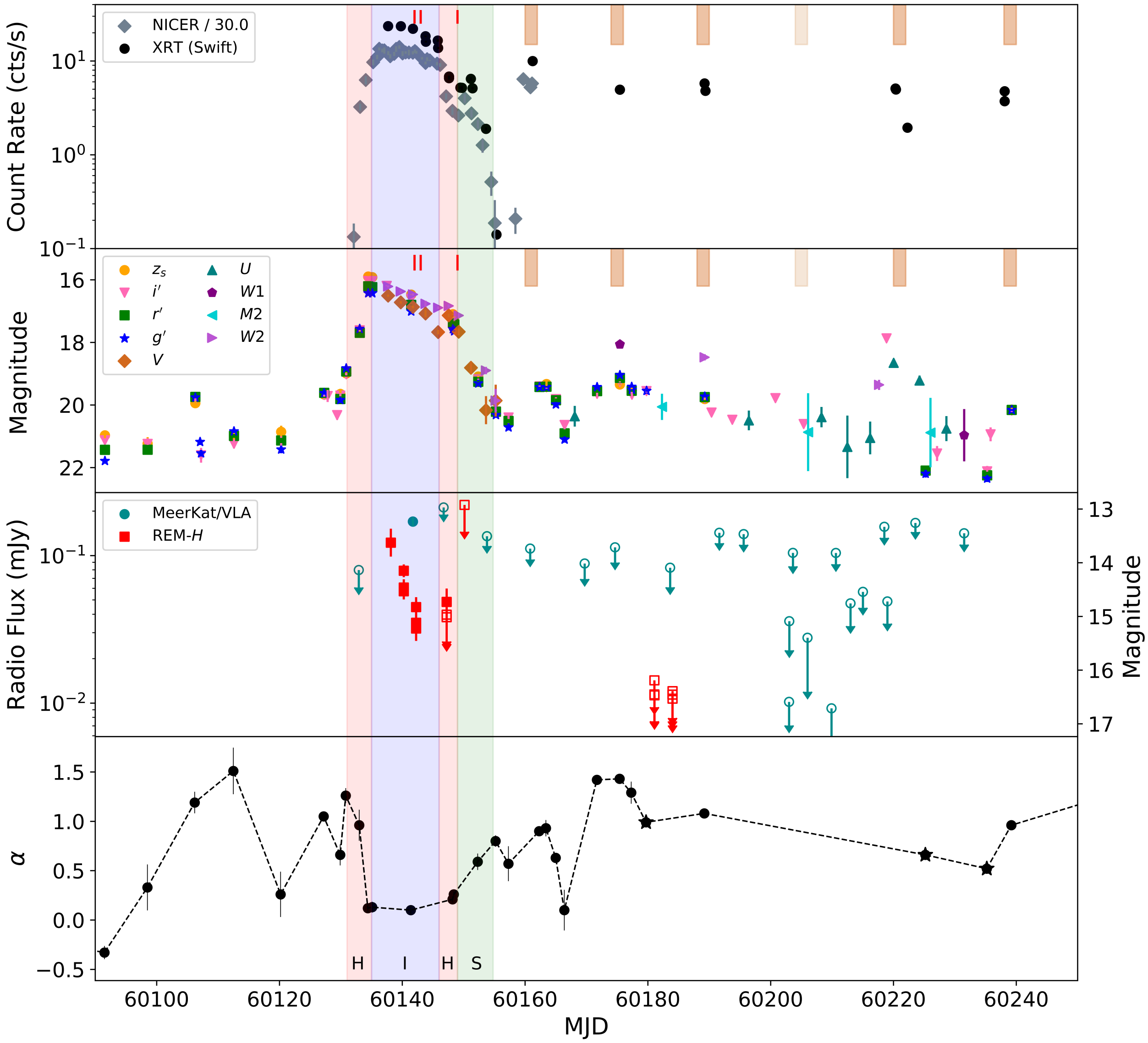

Figure 3. Top panel: X-ray lightcurves of MAXI J1807+132 with NICER (0.5–10 keV) and Swift/XRT (0.3–10 keV). The NICER lightcurve is reduced by a factor of 30 to plot it in the same frame as XRT. Second panel: Optical and UV lightcurves with LCO and Swift/UVOT, respectively. The light brown vertical bars dropping from the top in the first two panels represent the approximate epochs of the reflare peaks. The fourth epoch, marked ∼12 days after the previous reflare, has a lighter shade as the peak of the reflare is not well constrained. The red vertical lines in these two panels represent the epochs when the optical polarization measurements were done with VLT. Third panel: Radio lightcurve made with MeerKAT/VLA data and IR (H-band) lightcurve with REM data. Solid markers represent detections, whereas empty markers represent 3 × rms and 3σ upper limits for radio and IR bands, respectively. Bottom panel: Evolution of the spectral index (α) obtained by fitting the optical SED with a power law. The vertical patches that run across the four panels represent the boundaries of the spectral states as defined in S. K. Rout et al. (2025). The letters H, I, and S stand for the hard, intermediate, and soft states. The plateau phase discussed in this work broadly encompasses the intermediate state.

the main outburst. Before the optical activity began, during the quiescent stages, MAXI J1807+132 occupied the bottom right position with redder colors ($\alpha \lesssim 0$). With the optical rise, the source became bluer ($\alpha \gtrsim 0$) until MJD 60133.0, just before the outburst peak, when the color becomes slightly redder. In the following six observations, until MJD 60152.3, the colors remained significantly red. These observations stand out as a horn in the upper right part of each CMD (Figure 5). In the rest of the observations, the color evolution follows the normal diagonal track in the CMD.

We modeled the CMDs with a uniform-temperature blackbody of constant area as it cools and heats (D. Maitra & C. D. Bailyn 2008; D. M. Russell et al. 2011). The flux normalization of the model depends on several parameters such as the masses of the two stars, the size and inclination of the disk, the distance to the source, and other factors, most of which are degenerate and poorly constrained for MAXI J1807+132. Hence, the flux normalization is also poorly constrained, and we opted to use a multiplicative factor to overlap the model with the data. This factor is proportional to the projected area of the blackbody, which depends on the aforementioned uncertainties and which we assumed to remain constant. For UVOT filters, we used the same parameters, albeit with a different range of temperatures that is consistent with UV emission. It is interesting to note that the disk is already at a high temperature of ≈7500 K before the start of

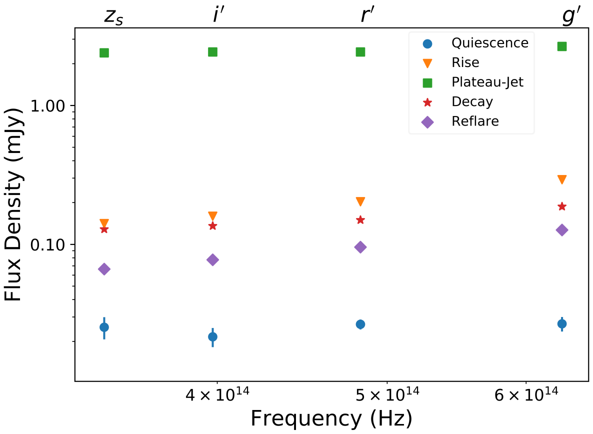

Figure 4. Five representative LCO SEDs during different stages of the outburst. The MJDs of the five epochs (from quiescence to reflare) are 60120, 60130, 60135, 60152, 60189.

the outburst. Before deviating toward redder colors from the blackbody track near the peak, the temperature increases to ≈24,500 K in the optical bands and to ≈30,000 K in the UV.

3.4. X-Ray–Optical/UV Correlations

We studied the correlation between the optical/UV and quasi-simultaneous X-ray fluxes to determine the dominant optical and UV emission mechanism (D. M. Russell et al. 2007). Of all available observations, data from six LCO epochs were found to be within 24 hr of an X-ray observation with NICER in the hard or intermediate states. Similarly, eight observations were found to be quasi-simultaneous between NICER and Swift/UVOT (only V and $W2$ filters) during the hard or intermediate states. Only one and two observations with LCO and UVOT, respectively, were found to be quasi-simultaneous with NICER during the soft state. Therefore, we did not carry out a correlation study in the soft state. The unabsorbed X-ray fluxes in the 2–10 keV range were calculated from spectral fits to the NICER data (S. K. Rout et al. 2025). The fluxes in both optical/UV and X-ray bands span about 2 orders of magnitude, and there is a clear positive correlation, albeit with significant scatter. We fit the correlations with a power law using the ODR algorithm.[24] Figure 6 shows the correlations for six optical/UV filters (LCO: z_s, i', r', g'; and UVOT: V, $W2$) along with the best-fit models (dashed lines). The power-law index, β ($F_{\rm opt/uv} \propto F_{\rm xray}^{\beta}$), monotonically increases with increasing wavelength of the optical/UV filters, although with large uncertainty. While it is 0.60 ± 0.08 for the $W2$ filter, it increases to 0.92 ± 0.31 for the z_s filter. There is systematically more scatter in the longer wavelength bands, which is evident from the corresponding levels of uncertainty (Figure 6).

We investigated the significance of the correlation between the wavelengths and β using a similar method as used in Section 3.1. First, we fit the correlation by a constant model and then by a line, with a nonzero slope and intercept, using χ^2 minimization. The $\Delta\chi^2$ between the two models is 2.22 for 1 additional degree of freedom, indicating that they are not significant at the 5% or 10% level. This suggests that while there may be a correlation, it is not highly significant.

3.5. Optical Polarization

The results of our analysis of the optical polarization observations performed with FORS2 are given in Table 2. The level of linear polarization, after the correction for the reference stars, is always $\leqslant 1\%$ in all bands and at all epochs. In the first epoch, P is constant at a level of ~0.6% at all frequencies, and the polarization angle, θ, is approximately constant at ~80° (with a slight but significant deviation in the I band). In the second epoch, P reduces at all frequencies, while θ maintains similar values. A significant variation in polarization is observed in the third epoch. The level of polarization becomes undetectable in the B and V bands, with constraining upper limits. In contrast, the P values in the R and I bands are significantly higher than those in the second epoch, with a swing in θ of ~100°[25] in both bands. This evolution of polarization properties in the three epochs can be visualized in Figure 7.

3.6. Radio Detection

Only one MeerKAT observation (2023 July 16, MJD 60141) showed significant evidence for radio emission originating from MAXI J1807+132 (shown in the second panel of Figure 8). For this detection, we extracted the source flux (with IMFIT) using a synthesized beam-shaped Gaussian. We measured the rms noise from a nearby source-free region using a circular extraction aperture with an area equal to ~100 synthesized beams. We observed an unusually large offset between the radio and optical positions (~3″). Comparably large astrometric errors have been seen in past comparisons of radio-infrared positions,[26] where group delay errors were found to be the most likely culprit; although not certain, it is possible that these errors also affect our radio observations. Regardless, the temporal coincidence of the detection with the peak of the outburst and the fact that the new component is at a different position from the three persistent sources are consistent with the source emission originating from MAXI J1807+132.

For the remaining nondetections, we performed forced aperture photometry by extracting the peak flux density using a synthesized beam-shaped Gaussian fixed at the optical position. Then we added the forced aperture flux densities and 3× the rms noise value and adopted these as 3σ flux upper limits. Therefore, our upper limits consider both noise-driven uncertainty and confusion from the nearby field sources. The radio fluxes of MAXI J1807+132 are shown in Figure 3.

4. Discussion

We conducted a multiwavelength analysis of the NS LMXB MAXI J1807+132 during its latest outburst in 2023, using data from several ground and space-based observatories. Thanks to the prompt initiation of X-ray observations following the optical rise, we were able to detect the X-ray rise early in the outburst. Despite some uncertainties, we detected a clear delay of ~4–12 days between the X-ray and optical rises. The outburst was characterized by a rapid rise, a gradual decay (the plateau phase), and, after a brief flare, a

---

[24] https://docs.scipy.org/doc/scipy/reference/odr.html

[25] This is if the electric field vector rotates in the anticlockwise direction. If the vector rotates instead in the clockwise direction, the swing in polarization will be ~75°.

[26] See obit development memo series no. 6: http://www.cv.nrao.edu/~bcotton/ObitDoc/SelfCalAstro.pdf.

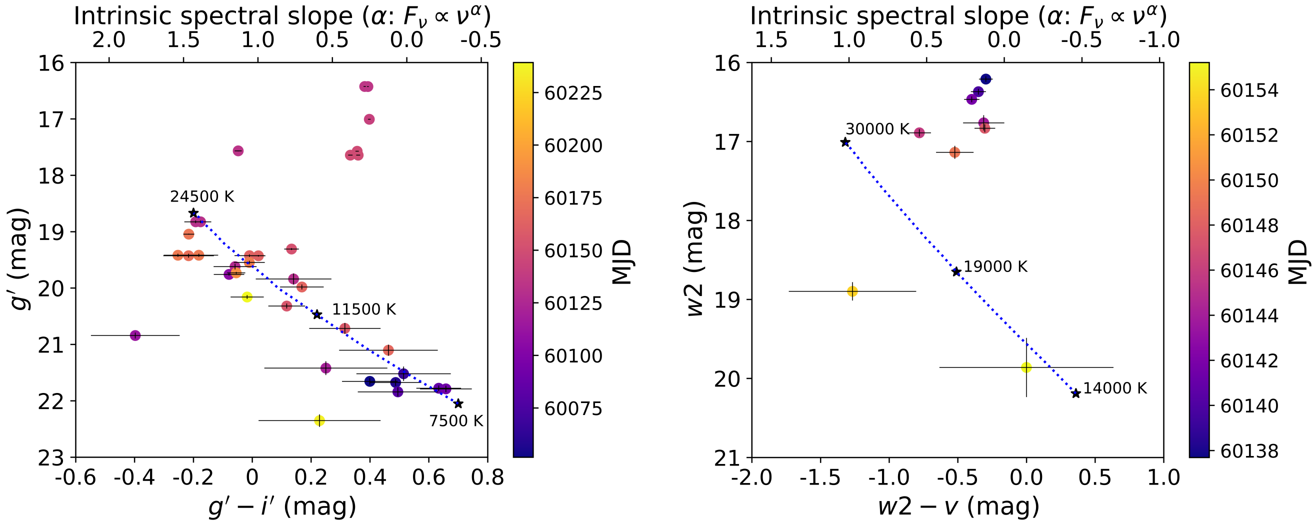

Figure 5. CMDs with LCO g' and i' filters (left) and UVOT $W2$ and V filters (right). The blue dotted lines represent a blackbody model with different temperatures. The temperatures at three representative positions on the models are marked with stars. The top x-axis shows the dereddened spectral slope.

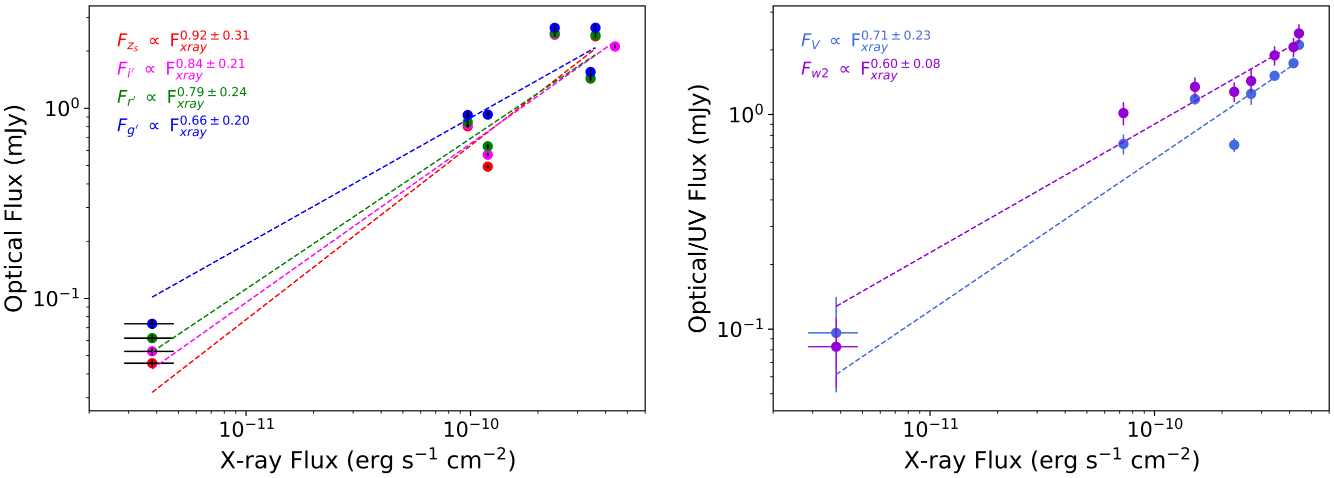

Figure 6. Left: X-ray/optical correlation with the four filters of LCO. Right: X-ray/optical-UV correlation with the two filters of UVOT. The unabsorbed X-ray flux is in the 2–10 keV range from fits to the NICER spectra. The dashed lines represent the best-fit power-law models.

Table 2
Results of the VLT/FORS2 (BVRI Filters) Polarimetric Campaign

Epochs	MJD	B		V		R		I	
		P (%)	θ (°)	P (%)	θ (°)	P (%)	θ (°)	P (%)	θ (°)
1	60142.1	$0.61^{+0.07}_{-0.09}$	$80.49^{+3.54}_{-3.44}$	$0.55^{+0.05}_{-0.06}$	$85.63^{+2.90}_{-2.83}$	$0.57^{+0.04}_{-0.05}$	$82.17^{+2.27}_{-2.26}$	$0.60^{+0.04}_{-0.05}$	$63.36^{+2.24}_{-2.10}$
2	60143.1	$0.29^{+0.07}_{-0.08}$	$99.09^{+7.09}_{-7.13}$	$0.34^{+0.05}_{-0.06}$	$83.24^{+4.47}_{-4.45}$	$0.51^{+0.04}_{-0.05}$	$75.88^{+2.51}_{-2.45}$	<0.17	$87.05^{+36.58}_{-34.54}$
3	60149.0	<0.56	$137.96^{+11.48}_{-13.19}$	<0.4	$144.42^{+16.07}_{-29.68}$	1.03 ± 0.06	$176.83^{+1.77}_{-1.79}$	0.63 ± 0.06	192.20 ± 2.75

Note. All of the polarization levels and angles are corrected for instrumental polarization. The interstellar polarization has also been subtracted, by means of a group of reference stars in the field. Upper limits are indicated at a 99.97% credible interval, and the rest of the uncertainties are $\pm 1\sigma$ credible intervals.

sharp drop to near-quiescence levels. We also detected signatures of jet synchrotron emission in the optical and infrared (OIR) bands throughout the plateau phase. Following the outburst, a series of high-amplitude reflares (∼2 orders of magnitude in flux), with a quasi-periodicity of $\gtrsim$12 days, occurred over a period of three months.

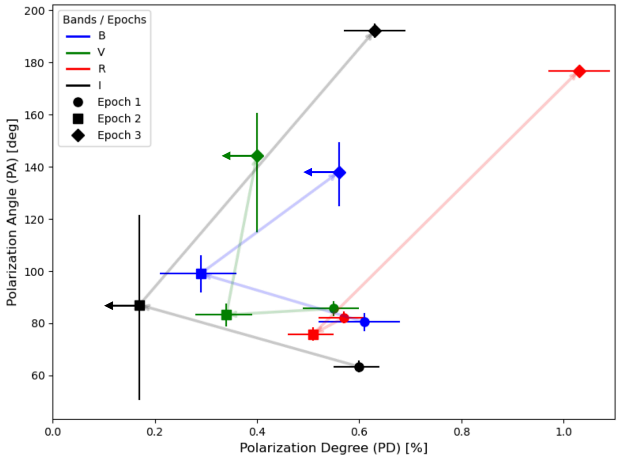

Figure 7. Optical polarization degree (P) vs. polarization angle (θ) for the three epochs. A clear rotation of θ by approximately ∼100° is observed in the R and I bands between the first two epochs and the third. Upper limits on P are reported at the 99.97% credible interval, while all other uncertainties are quoted at the $\pm 1\sigma$ credible level.

4.1. Optical Precursor and X-Ray Delay

MAXI J1807+132 undergoes a slow and long-term rise during the quiescence that began ∼400 days before the main outburst (Appendix C). This long-term trend is expected from the DIM as matter accumulates gradually in the accretion disk, leading to an increase in surface density and temperature (e.g., G. Dubus et al. 2001). The rise rates for the bluer bands (∼0.3 mag yr^{-1}) are steeper than those for the redder bands (∼0.1 mag yr^{-1}), consistent with previous observations of LMXBs (e.g., F. Bernardini et al. 2016; K. I. I. Koljonen et al. 2016). A precursor to the main outburst was detected on MJD 60106.2, that is, ∼26 days before the first X-ray detection. This enhanced optical flux, however, decayed down to near-quiescent levels for a couple of weeks. The commencement of the fast optical rise, when the heating wave sweeps through the disk, likely began somewhere between MJD 60120.2 and 60127.2, that is, about 4–12 days before the X-ray rise. The precursor delay (∼26 days) is too long to be associated with viscous timescales of the disk, which are of the order of a few days. It probably appears as a result of some other activity that leads to the enhanced accretion in the next 15 days. Such a precursor was also detected in the accreting millisecond pulsar SAX J1808.4–3658 12 days before an optical rise (A. J. Goodwin et al. 2020). This suggests that the precursor could be a generic feature of LMXB outbursts, although their origin is unclear. It is unlikely to be similar to the misfired outburst in Cen X-4 (M. C. Baglio et al. 2022), where the temperature does not reach the hydrogen ionization level. In both MAXI J1807+132 (Figure 5) and SAX J1808.4–3658 (M. C. Baglio et al. 2020) the disk temperature exceeded ∼7000 K. One possibility could be an enhanced mass transfer due to some stellar activity in the companion, which results in an optical flare. Alternatively, some instabilities can arise due to the impact of the accretion stream or from spiral waves in a dense outer disk, resulting in optical activity.

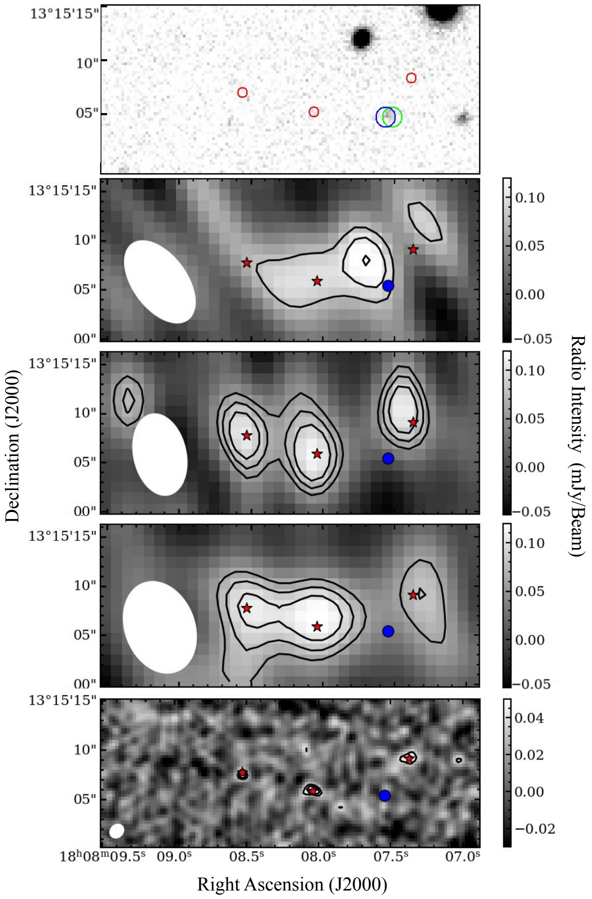

Figure 8. Multifrequency images of MAXI J1807+132 and the surrounding region. The top panel shows an optical (i'-band) image taken with the LCO on 2024 August 2 (MJD 60524); the second panel shows a MeerKAT (∼1.3 GHz) image taken on 2023 July 16 (MJD 60141); the third panel shows a MeerKAT (∼1.3 GHz) image taken on 2023 July 28 (MJD 60153); the fourth panel shows a MeerKAT (∼1.3 GHz) image taken on 2023 September 4 (MJD 60191); the bottom panel shows a VLA (∼1.5 GHz) image taken on 2023 October 2 (MJD 60219). The contours in the four radio images represent 3σ, 4σ, and 5σ levels. The open red circles and solid red stars show the radio positions of the field sources in the optical and radio images, respectively. Similarly, the open blue circle and the solid blue circle show the optical position of the source in the optical and radio images, respectively. The open green circle in the optical image corresponds to the UVOT position of the source. The noise levels for the four radio images, from top to bottom, are 27, 18, 20, and 13 μJy beam^{-1}. The three field sources are consistent with having constant fluxes in the four epochs, to $<2\sigma$ of the mean level. The first MeerKAT image shown in the second panel corresponds to the only radio detection of MAXI J1807+132.

One key observable of the DIM is the delay between the rise in X-ray and optical flux at the beginning of an outburst. According to the DIM, the outburst begins when, due to increasing viscosity, the disk temperature rises to a level where hydrogen starts to ionize, that is, $\gtrsim$6500 K. This is a temperature at which a blackbody peaks in the blue region of the optical spectrum. As the heating front reaches the inner disk, the temperature increases to levels where X-rays are emitted. However, even before the direct disk emission, the X-rays start to emanate because of Comptonization of the optical/UV emission in the hot flow. Therefore, the rise of X-ray emission is delayed with respect to the rise of optical (blue) emission at the beginning of the outburst. The exact duration of the delay, however, depends on a number of factors related to the time it takes (1) the heating wave to travel from the ignition radius to the inner disk, (2) the inner disk to propagate toward the NS, and (3) the mass accretion rate to rise in the hot flow. If the ignition occurs at a smaller radius, then the heating front reaches the inner disk faster than in the case where the ignition occurs at a larger radius. These two cases are termed inside-out and outside-in outbursts, respectively (G. Dubus et al. 2001). However, this does not imply that inside-out outbursts have a smaller delay (J. M. Hameury 2020).

Determining the type of outburst, that is, inside-out or outside-in, requires constraining the ignition radius, which depends on the size of the disk and the mass transfer rate from the companion, both of which are quite difficult to constrain (J. Smak 1984). Moreover, the 4–12 days' delay between the X-ray and optical rise measured in MAXI J1807+132 is much greater than the time it takes for the heating to reach the inner edge of the disk, no matter where it originates in the disk. For instance, the heating front could take less than a day to reach the inner edge if it is an inside-out outburst and/or if it is a short-period system. The delay is also a function of the viscosity parameter (J. M. Hameury et al. 1997). Delays of the order of a few to several days can be explained if the disk is truncated at the beginning of the outburst, due to either magnetic pressure (M. Livio & J. E. Pringle 1992) or evaporation (F. Meyer & E. Meyer-Hofmeister 1994). The heating front would then have to stop at the truncated inner edge of the disk, which would then move inward at a viscous timescale, which is longer than the propagation time of the heating front (K. Menou et al. 1999; G. Dubus et al. 2001). From the X-ray study of the source, it was indeed found that the disk was highly truncated at the beginning (S. K. Rout et al. 2025). Viscous timescales for the propagation of matter or turbulence from the optical to X-ray-emitting region have been attributed to a few BH LMXBs, namely, GRO J1655–40 (6 days; J. M. Hameury et al. 1997), LMC X-3 (5–10 days; C. Brocksopp et al. 2001), GX 339–4 (15–20 days; J. Homan et al. 2005), XTE J1118+480 (>4 days; C. Zurita et al. 2006), 4U 1957+11 (2–14 days; D. M. Russell et al. 2010), Swift J1910.2–0546 (6 days; N. Degenaar et al. 2014; P. Saikia et al. 2023c), and so on. However, it is important to note that the viscous timescales measured in these studies were done during the outburst, when the whole disk is ionized and the timescale is dominated only by the viscous timescale. This is not directly comparable with the delays of the X-ray rise at the start of the outburst, which depend on many other factors that were mentioned above.

4.2. UV-Optical-IR (UVOIR) Emission Processes

The outburst of MAXI J1807+132 shows a very fast rise, so much so that it reaches the peak about two days after its first detection in X-rays. Figure 3 shows the boundaries of the spectral states as defined in S. K. Rout et al. (2025) on the multi–wave band lightcurves with different colors. The source transitions from the hard state to the intermediate state between the peak and the end of the gradually declining plateau phase on MJD 60146. Following this, the state becomes hard for a few days, marked by a sudden drop in flux and an increase in the X-ray variability and hardness. On MJD 60150, the source transitions to the soft state with a short flare in the X-rays. The optical/UV lightcurves also follow the same trend as the X-ray lightcurve, although the decay in the intermediate state is slightly shallower than the X-ray decay. It is during the intermediate and hard states between MJD 60134 and 60150 that we detected signatures of jet synchrotron emission at optical wave bands. The OIR emission may have contributions from the accretion disk (viscous or irradiated), secondary star, hot spots, hot flow, or jet, making the identification of the dominant mechanisms difficult (N. I. Shakura & R. A. Sunyaev 1973; C. Cunningham 1976; J. van Paradijs & J. E. McClintock 1994; S. Corbel & R. P. Fender 2002; D. M. Russell et al. 2006; A. Veledina et al. 2013). Therefore, we employed a number of diagnostic tools to identify the emission mechanism, which are discussed below.

4.2.1. Color Evolution—SED and CMD

We fit optical SEDs with a power law ($F_\nu \propto \nu^\alpha$) parameterized by the spectral index, α, along with a normalization. The evolution of the spectral index is shown in Figure 3. Although for most of the outburst, the SEDs are bluer (i.e., steeper with $\alpha \approx 1.0$) when brighter, they become flat ($\alpha \approx 0$) during the plateau phase. The steep spectral indices during the rise and reflare peaks are consistent with the disk emission, both viscous and irradiated (R. I. Hynes 2005). The shallow index range (~0–0.4) at the peak and initial decay (plateau), on the other hand, is consistent with a multi-temperature blackbody from the viscous accretion disk (where $\alpha \sim 1/3$ is expected) or a self-absorbed jet (which can be flat or slightly inverted; $\alpha \sim$ 0–0.5 e.g., R. P. Fender et al. 2001; D. M. Russell et al. 2013b; T. D. Russell et al. 2014). If the flattening in the SED is caused by the disk emission, then the temperature must be lower than that measured. This becomes apparent from the CMD modeling, as discussed in the following.

The reddening of the spectral index detected in the SEDs also becomes apparent in the CMD. The $g'-i'$ color starts to deviate from the diagonal track and becomes redder just before reaching the peak of the outburst (Figure 5). Although UVOT missed the rise of the outburst, it started observing from the peak until the end of the main outburst. Quite remarkably, the UVOT CMD also shows that the $W2 - V$ color is considerably red near the peak and moves toward bluer colors as the outburst decays (Figure 5). The diagonal track can be modeled by a blackbody function, and it is represented by a blue dotted line. The points along this model are dominated by the irradiated disk emission, whereas the outlier points have a significant contribution from some other source (e.g., D. M. Russell et al. 2011). This is based on the principle that for an irradiated disk scenario the optical emission is dominated by different parts of the Planck's blackbody function at different temperatures. At low temperatures, the optical emission comes from the peak or the Wien's tail, hence a flat or red SED (high $g'-i'$), while at higher temperatures the emission is dominated by the Rayleigh–Jeans tail, resulting in a bluer SED (low $g'-i'$). Whenever there is a significant contribution from any other source, the observed colors tend to deviate from the model. It has often been seen that a significant contribution from jet synchrotron emission results in a redward shift of the colors away from the blackbody track (e.g., M. C. Baglio et al. 2020). The six points in MAXI J1807+132 starting at the peak of the outburst (top right corner in Figure 5 between MJD 60134.4 and MJD 60152.3) represent such an excursion possibly arising from the jet.

4.2.2. X-Ray versus Optical/UV Correlation

If the UVOIR emission is dominated by the viscous disk, then the correlation index $\beta \sim 0.3$ ($F_{\rm opt} \propto F_{\rm xray}^{\beta}$). For an irradiated disk, this would be $\beta \sim 0.5$ (J. van Paradijs & J. E. McClintock 1994;

J. Frank et al. 2002). D. M. Russell et al. (2006) found a global OIR/X-ray correlation index of ∼0.6 for both NS X-ray binaries (NSXBs) and BH X-ray binaries (BHXBs) in the hard state. This correlation can be adequately explained by an X-ray reprocessing model for BHXBs, and also for NSXBs at low luminosities. At luminosities $\gtrsim 10^{36}$ erg s^{-1}, the jet may dominate the OIR flux for atoll sources (D. M. Russell et al. 2007). There have not been many studies dedicated to finding a correlation when the OIR flux is dominated by jet emission. This correlation would be similar to the radio/X-ray correlation if the optically thick part of the synchrotron spectrum is flat and the spectral break occurs at higher frequencies, that is, in the optical regime (e.g., M. Díaz Trigo et al. 2018). Several studies have been dedicated to finding a radio/X-ray correlation, and a range of values have been estimated over the years. S. Migliari & R. P. Fender (2006) found a very steep radio/X-ray correlation of 1.4. E. Gallo et al. (2012), on the other hand, reported a bimodality in slopes corresponding to radio-loud ($\beta \sim 0.6$) and radio-quiet ($\beta \sim 1$) jets. E. Gallo et al. (2018) even reported a shallower slope of 0.71 for atolls, and even a lower value of 0.44 for all NSXBs. Probably limited by detection sensitivities, there seems to be no global radio/X-ray correlation in NSXBs (e.g., V. Tudor et al. 2017; J. van den Eijnden et al. 2021). Moreover, NSs are inherently more complex than BHs owing to a surface that spins and anchors magnetic fields, which can result in more scatter in correlations.

The studies done so far suggest that the correlation between UVOIR and X-ray flux becomes steeper (i.e., increases from ∼0.3 to 1.4) as one moves from a viscous disk to an irradiated disk and then to jet emission. For instance, the mid-IR flux, dominated by jet emission, was recently found to correlate with the X-ray flux with a steep $\beta \sim 0.82$ (C. John et al. 2024). The correlation indices for MAXI J1807+132 in the $W2$, g', and V bands ($\beta \sim 0.6$) are consistent with X-ray reprocessing. The longer wavelength bands (r', i', and z_s), on the other hand, show a somewhat steeper correlation with X-rays ($\beta \gtrsim 0.6$). This suggests a possible contribution of the jet in the r', i', and z_s bands. As shown in Section 3.4, although not highly significant, there is a hint of a positive correlation between β and wavelength that is opposite to that expected from a viscous heated disk (e.g., M. Armas Padilla et al. 2013; A. Patruno et al. 2016).

4.2.3. Infrared and Radio Detections

During the hard and intermediate states of X-ray binaries (XRBs), outflows in the form of jets are usually detected, and these jets are then quenched by about 3 orders of magnitude as the source transitions to a soft state (e.g., T. D. Russell et al. 2014; F. Carotenuto et al. 2021). Jet emission is clearly identified at radio wavelengths, while its contribution in the millimeter and IR regimes is also well known (e.g., S. K. Rout et al. 2021). Our radio observation campaign with MeerKAT and VLA results in a detection at the source position (Figure 8) during the intermediate state on MJD 60141 (2023 July 16). This is the only significant detection of the 22 observations. Moreover, observations in the H band carried out with REM reveal strongly variable emission during the intermediate and hard states (Figure 3). The radio detection and variability of the IR emission during the plateau phase of the outburst likely results from a brightened jet, which would, in turn, also explain the reddening of the optical color.

As the radio flux at ∼0.17 mJy is about a factor of 10 below the IR and optical flux, the optically thick component of the synchrotron emission is inverted. Due to the lack of data in the mid-IR wave bands, it is not possible to constrain the break frequency. However, assuming the z_s band represents the upper limit on the break frequency, we find the spectral index of the optically thick component to be $\gtrsim 0.18$. The optically thin component has a negative spectral index ~ -0.7. This suggests that the jet spectrum possibly curves to become flat somewhere in the IR, implying the break to be close to the IR/optical bands (e.g., P. Gandhi et al. 2011).

4.2.4. Optical Polarimetry

There are several potential sources of optical polarization in XRBs. First, the disk emission may be polarized up to 12% depending on the inclination, and the polarization angle can vary with the opacity of the atmosphere, switching by ∼90° between the optically thin and thick cases (S. Chandrasekhar 1960; R. A. Sunyaev & L. G. Titarchuk 1985). Second, synchrotron emission from the jet can be polarized up to 70%–75% depending on the slope of the electron distribution and the level of ordering of the magnetic field lines in the jet (G. B. Rybicki & A. P. Lightman 1979). The resulting linear polarization in the total emission of the XRB will, however, strongly depend on the fractional contribution of the jet to the optical flux, which varies depending on the source and on the time of the observation. In addition, synchrotron emission from a hot flow can give a small polarization (up to a few percent) if the magnetic field in the hot flow has an ordered component (A. Veledina et al. 2013). Although the expected polarization from various mechanisms is well understood theoretically, it is often difficult to disentangle the individual components.

Our polarization measurements of MAXI J1807+132 with FORS2/VLT suggest an interesting scenario. Of the three epochs of observations (Figure 7), the first two were acquired during the intermediate state, while the last one was obtained during the hard state. From the previous analyses (Sections 4.2.1 and 4.2.2), we found that the jet spectrum possibly extends to the optical wave bands and could therefore be responsible for the observed linear polarization. In accordance with this scenario, the polarization spectrum is flat, imitating the flat OIR flux spectrum of the jet. On the other hand, if the polarization were caused by electron scatting in the disk, it should have increased toward bluer frequencies. Such low levels of OIR polarization from the jet are a strong indication of tangled magnetic fields at the base of the jet, as is typically observed in most XRBs (see, e.g., D. M. Russell 2018; M. C. Baglio et al. 2020).

The third epoch, during the excursion to the hard state, saw a dramatic change in polarization. While P could not be constrained in the B and V bands, it increased to 1.03% ± 0.06% and 0.63% ± 0.06% in the R and I bands, respectively. Moreover, θ rotated by ∼100° compared to the previous epochs. It is interesting to note that this third observation was made just before (<1 day) the short X-ray flare on MJD 60150, after which the source transitioned to the soft state. In BHXBs, transitions from the hard intermediate state to the soft intermediate state are often accompanied by X-ray brightening and/or discrete ejection of ballistic jets. In this circumstance, compression of the magnetic field lines in shocks within the jet might occur, generating partially ordered transverse magnetic fields (as observed in the case of the BHXB V404 Cyg; T. Shahbaz et al. 2016). This can explain the roughly orthogonal rotation of θ in the third epoch as compared to the first two epochs. Moreover, a discrete ejection would also imply an optically thin synchrotron emission, that is, a red spectrum, with stronger polarization at longer wavelengths, as observed (Figure 7). Incidentally, the rotation of θ by 90° during the transition has only been observed at radio wavelengths (e.g., P. A. Curran et al. 2014, 2015). Therefore, MAXI J1807+132 could be the first XRB to display a similar swing in θ in the OIR wave bands associated with the state change (and in this case, a flare), which could potentially be due to the quenching of the compact jet and the ejection of the ballistic jet during the hard-to-soft transition.

4.3. Reflares

Outbursts of XRBs, as well as those of accreting white dwarfs in dwarf novae, often exhibit rebrightening episodes during and/or after the end of the main outburst (e.g., W. Chen et al. 1993, 1997). Depending on a rebrightening's amplitude, shape, duration, and position in the lightcurve, it can be classified as a glitch, a reflare, or a mini outburst (see G. B. Zhang et al. 2019 for a detailed classification scheme). The rebrightenings in MAXI J1807+132 appear to start before the main outburst returns to quiescence, and their peak brightness remains less than 70% of the peak brightness of the main outburst, so we classify them as reflares (Figure 3).

The high amplitude and short duration of the reflares are one of the most unusual aspects of this source, seldom seen in other NSXBs. The peak brightness of these reflares in both the X-ray and optical/UV bands rises by ∼2 orders of magnitude above the quiescent levels (Figure 3). Not only is the amplitude high, the source also reaches the peak flux levels rapidly, in ∼2–4 days, matching the rapid rise of the outburst onset. Some sources like Swift J1858.6−0814 show numerous short-timescale reflares, but they are of low amplitude ($\lesssim$1 mag L. Rhodes et al. 2024). Then there are other sources like IGR J00291+5934, which show large-amplitude reflares, but they are of long duration and few (F. Lewis et al. 2010). The high amplitudes and short duty cycles of the reflares in MAXI J1807+132 make it difficult to explain theoretically (see A. Patruno et al. 2016, for reflares in SAX J1808.4–3658, which are similar to MAXI J1807+132).

Reflares that occur near in time, or just after, the main outburst pose a challenge for the DIM as at this stage the disk is almost depleted of matter. The propeller effect has been invoked in this regard and can halt the disk from emptying itself near the end of an outburst, thereby maintaining a matter reservoir for further accretion events (J. M. Hartman et al. 2011; A. Patruno et al. 2016). It has also been suggested that a hot nonstandard, or trapped, disk can exist toward the end of the outburst that accretes matter at low levels (A. Patruno et al. 2016; G. B. Zhang et al. 2019; V. A. Cúneo et al. 2020). However, a strong propeller regime is disfavored by S. K. Rout et al. (2025), as strong magnetic fields would result in very little accretion onto the NS surface. Since the radius of the inner disk often reaches the last stable orbit, a weak propeller or a trapped disk scenario is considered more likely (S. K. Rout et al. 2025). In this configuration, the inner parts of the disk deviate from the standard thin-disk solution and low levels of episodic accretion persist on the NS surface (A. Patruno et al. 2016).

An alternative explanation from the DIM is that reflares could be caused by multiple reflections of the heating and cooling fronts whenever they encounter a density gradient (J.-P. Lasota 2001). This process was invoked to explain the reflares in the BHXB Swift J1910.2–0546 (P. Saikia et al. 2023c). However, the CMDs for MAXI J1807+132 (Figure 5) imply that the disk temperature always remained in the hot branch (>7000 K), even at g'∼22 mag, which is inconsistent with the idea of traversing heating/cooling fronts. Irradiation of the outer accretion disk could keep the disk in the hot branch and prevent quiescence from setting in (A. R. King & H. Ritter 1998). The high values of the OIR spectral index ($0.75 \lesssim \alpha \lesssim 1.4$) during the reflare peaks suggest sustained irradiation of the outer disk as a viable mechanism. The repeating nature of the reflares can then arise due to the heating of the companion star that results in an enhanced mass transfer in a quasi-periodic manner, or similar "echoes" from an earlier enhanced accretion event (T. Augusteijn et al. 1993).

Outflows have also been proposed as an explanation for reflares in XRBs. The OIR reflares in BHXBs are sometimes caused by jet emission after the transition to the hard state (e.g., M. M. Buxton & C. D. Bailyn 2004; E. Kalemci et al. 2013). However, this is unlikely to be the case for MAXI J1807+132 as the emission at the reflaring stage is dominated by the irradiated disk. A jet, if present, would be fainter than the disk to be directly detected.

5. Summary

The NS atoll MAXI J1807+132 went into an outburst in 2023 July. We observed the source in radio, IR, optical, UV, and X-ray wave bands. The main findings of our study are as follows:

1. The optical rise was detected about 4–12 days before the X-ray rise. Such a delay is consistent with a truncated disk scenario where the heating front first reaches the disk edge, which then moves toward the compact object on viscous time scales to produce X-rays.
2. After reaching the peak of the outburst, in the intermediate and hard state, the presence of jet is supported by radio and IR detection. The jet synchrotron emission probably also dominates the optical wave bands as evidenced from the evolution of optical color and SEDs.
3. The power-law indices of the correlations between the X-ray and UVOIR fluxes are high ($\beta \sim$ 0.6–0.9). Steep correlations are detected at longer wavelengths (i.e., r', i', and z_s bands), suggesting a possible contribution of the jet.
4. Optical polarization measured with the VLT showed low levels of polarization ($\lesssim$1%) in the first two epochs. The third epoch, just before an X-ray flare, saw a rotation of the polarization angle by ∼100° in the R and I bands. This could be related to an ejection of material associated with the flare.
5. The main outburst is followed by a series of high-amplitude rapid reflares in the optical, UV, and X-ray wave bands. The reflare SEDs suggest a reprocessed disk emission in the optical/UV wave bands, but their color temperatures are inconsistent with traveling heating/cooling fronts.

Acknowledgments

The authors acknowledge constructive feedback from the referee. This research is based on work supported by Tamkeen under the NYU Abu Dhabi Research Institute grant CASS.

This research has made use of data and/or software provided by the High Energy Astrophysics Science Archive Research Center (HEASARC), which is a service of the Astrophysics Science Division at NASA/GSFC. This work made use of data supplied by the UK Swift Science Data Centre at the University of Leicester. This research is based on observations collected at the European Southern Observatory under ESO program 111.24K2. M.C.B. acknowledges support from the INAF-Astrofit fellowship. T.M.D. acknowledges support by the Spanish Ministry of Science via the Plan de Generacion de conocimiento PID2021-124879NB-I00. J.H. acknowledges support through NASA grant 80NSSC23K1659. M.A.P. acknowledges support through the Ramón y Cajal grant RYC2022-035388-I, funded by MCIU/AEI/10.13039/501100011033 and FSE+. N.M. acknowledges financial support through ASI-INAF agreement 2017-14-H.0 (PI: T. Belloni). J.v.d.E. acknowledges a Warwick Astrophysics prize postdoctoral fellowship made possible thanks to a generous philanthropic donation and was supported by funding from the European Union's Horizon Europe research and innovation program under the Marie Skłodowska-Curie grant agreement No. 101148693 (MeerSHOCKS) for part of this work. J.H. acknowledges support through NASA grant 80NSSC24K0809.

Facilities: NICER, Swift (XRT and UVOT), LCOGT, VLT: Antu, REM, VLA, MeerKAT.

Software: Astropy (Astropy Collaboration et al. 2022), Scipy (P. Virtanen et al. 2020), Numpy (C. R. Harris et al. 2020), Matplotlib (J. D. Hunter 2007).

Appendix A
Optical Polarimetry with VLT

To determine the linear polarization of MAXI J1807+132, we applied the algorithm described by M. C. Baglio et al. (2020) and references therein. This method begins by calculating the parameter $S(\Phi)$ for each HWP angle:

$$S(\Phi) = \left(\frac{f^o(\Phi)/f^e(\Phi)}{f_u^o(\Phi)/f_u^e(\Phi)} - 1\right) \bigg/ \left(\frac{f^o(\Phi)/f^e(\Phi)}{f_u^o(\Phi)/f_u^e(\Phi)} + 1\right), \quad \text{(A1)}$$

where $f^o(\Phi)$ and $f^e(\Phi)$ are the ordinary and extraordinary fluxes of MAXI J1807+132, respectively, and $f_u^o(\Phi)$ and $f_u^e(\Phi)$ are the corresponding values for an unpolarized standard star in the field. This parameter is related to the target's polarization degree (P) and polarization angle (θ) by the equation:

$$S(\Phi) = P\cos 2(\theta - \Phi). \quad \text{(A2)}$$

Therefore, a fit of the S parameter with Equation (A2) will give an estimate of the linear P and θ for the target. To increase the significance of the fit, we considered six reference field stars in each epoch. Under the simple hypothesis that the field stars are intrinsically unpolarized, this method gives as a result a linear polarization for the target that is already corrected for the low instrumental effects. Moreover, if the field stars are polarized due to interstellar dust, this method should, in principle, automatically correct for interstellar polarization along the line of sight.

Following M. C. Baglio et al. (2020), to evaluate P and θ we maximized the Gaussian likelihood function using an optimization algorithm (e.g., the Nelder–Mead algorithm; F. Gao & L. Han 2012) and integrated the posterior probability density of our model parameters using a Markov Chain Monte Carlo algorithm (D. W. Hogg & D. Foreman-Mackey 2018) based on the "affine-invariant Hamiltonian" algorithm (D. Foreman-Mackey et al. 2013). The chains were initiated from small Gaussian distributions centered on the best-fit values. We discarded the first third of each chain as the "burn-in phase" and ensured that a stationary distribution was reached (S. Sharma 2017). The quality of the fit was assessed as described in L. B. Lucy (2016). The values for P and θ, along with their 1σ uncertainties, correspond to the 0.16, 0.50, and 0.84 quantiles of the posterior distribution of the parameters. In the case of nondetections, the 99.97% percentile of the posterior distribution of the parameter P was used to estimate an upper limit. The value of θ derived using this method was further adjusted based on observations of the polarized standard star BD-12 5133 (observed during the night of 2023 July 22 with the same setup as that of our observations), with known and documented polarization angles in all FORS2 bands (L. Fossati et al. 2007). The average correction applied was negligible, remaining under 2° across all bands and epochs.

Appendix B
VLA Campaign

The apparent temporal variability observed with MeerKAT was initially believed to be due to the discrete jet ejections common to both BH (e.g., X. Han & R. M. Hjellming 1992; R. M. Hjellming & M. P. Rupen 1995; A. J. Tetarenko et al. 2017; J. S. Bright et al. 2020) and (Z source) NS LMXBs (e.g., E. B. Fomalont et al. 2001; R. E. Spencer et al. 2013, although they are significantly less than BHs). To confirm the existence of the jets, we were approved for director's discretionary time observations (Project Code: VLA/23B-302) with the VLA. At the time, the VLA was in its most extended A configuration, resulting in a factor of ~5 improvement in angular resolution compared to MeerKAT (at L band). We acquired nine VLA observations: eight 8 bit L-band observations (~1.5 GHz, ~1 GHz bandwidth) between 2023 September 15 (MJD 60202) and 2023 October 9 (MJD 60226) and a single 3 bit C-band observation (~6 GHz, ~4 GHz bandwidth) at the same epoch as with the first L-band observation. During the last two (L-band) observations, the VLA moved into a hybrid configuration (A → D), significantly increasing the background flux density and, thus, noise levels; the increase in background was due to D configuration's sensitivity to large-scale extended emission. As a result, we do not use the last two VLA observations.

We processed the VLA data with the CASA pipeline (v6.4; CASA Team et al. 2022). For each observation, we passed the data through twice; after the first round of calibration, we inspected the visibilities, manually flagging any residual corrupted data and rerunning the pipeline. Following calibration, we adopted the OXKAT imaging workflow, producing one continuum image per VLA epoch.

The high-resolution VLA observations revealed our initial interpretations were incorrect, that is, the radio morphology did not result from jet ejecta. Instead, we discovered three moderately variable (~100 μJy with ~30% excess variances) but unassociated point sources within ~10″ of MAXI J1807+132 (see Figure 8). The apparent motion was due to MeerKAT's inadequate angular resolution combined with the variability of the three field sources, leading to confusion about the morphological evolution of MAXI J1807+132. We used the CASA task IMFIT to measure the positions of each source in each VLA observation, enforcing that each source adopts the shape of the synthesized beam. Below, we present the inverse-variance weighted average positions and errors using $>4\sigma$ detections (with the VLA):

Source 1: $18^{\mathrm{h}}08^{\mathrm{m}}08\overset{\mathrm{s}}{.}528$ $+13°15'07''.77$ ($\pm0''.08$)

Source 2: $18^{\mathrm{h}}08^{\mathrm{m}}08\overset{\mathrm{s}}{.}040$ $+13°15'05''.87$ ($\pm0''.05$)

Source 3: $18^{\mathrm{h}}08^{\mathrm{m}}07\overset{\mathrm{s}}{.}373$ $+13°15'09''.13$ ($\pm0''.17$).

In addition to the astrometric errors from IMFIT (which follow J. J. Condon 1997; J. J. Condon et al. 1998), we added, in quadrature, a systematic astrometric error equal to 10% of the (major-axis) FWHM of the synthesized beam.[27] We investigated the accuracy of our errors utilizing a nearby ($18^{\mathrm{h}}08^{\mathrm{m}}22\overset{\mathrm{s}}{.}455$ $+13°17'26''.129$) ~3 mJy field source, comparing our measured position to the positions fit using the VLA Sky Survey (VLASS) quick-look images.[28] The offsets of the check source in our images (compared to VLASS) are $<0''.05$ and have a uniform distribution of offset position angles (i.e., the direction of the offset, measured East of North). Given that our adopted astrometric systematic error is $>0''.1$ for all epochs, our estimated astrometric errors are reasonable, if not overly conservative. Future radio monitoring campaigns of MAXI J1807+132 need to compensate for the associated field sources; the MeerKAT *S*-band receivers or the VLA in A configuration have sufficient angular resolution to mitigate source confusion.

Appendix C
Supplementary Figure: Fits to Long-term Lightcurve

Figure 9 shows the long-term light curves of MAXI J1807+132 along with the best-fit model M3 (see Section 3.1 for details).

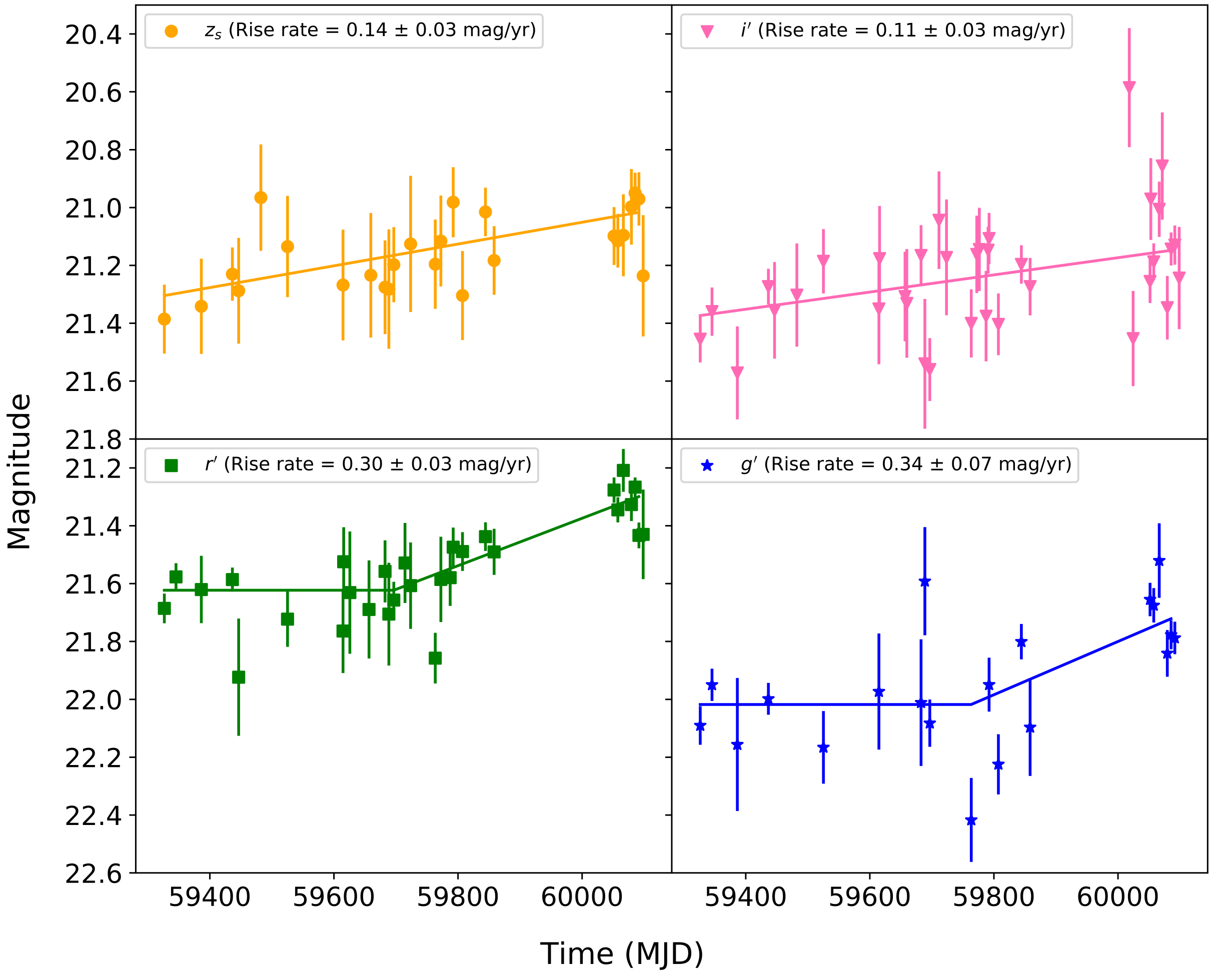

Figure 9. Fits to the long-term quiescent lightcurves of MAXI J1807+132 with the slow rise model. The color and symbols for different panels are the same as in Figure 1. The legends also mention the rise rates for the different filters.

---

[27] This systematic error follows the VLA recommendation: https://science.nrao.edu/facilities/vla/docs/manuals/oss/performance/positional-accuracy.

[28] The quick-look image server can be found here: http://cutouts.cirada.ca/.

ORCID iDs

Sandeep K. Rout https://orcid.org/0000-0001-7590-5099
M. Cristina Baglio https://orcid.org/0000-0003-1285-4057
Andrew K. Hughes https://orcid.org/0000-0003-0764-0687
David M. Russell https://orcid.org/0000-0002-3500-631X
D. M. Bramich https://orcid.org/0000-0002-1583-6519
Payaswini Saikia https://orcid.org/0000-0002-5319-6620
Kevin Alabarta https://orcid.org/0000-0003-0168-9906
Montserrat Armas Padilla https://orcid.org/0000-0002-4344-7334
Sergio Campana https://orcid.org/0000-0001-6278-1576
Stefano Covino https://orcid.org/0000-0001-9078-5507
Paolo D’Avanzo https://orcid.org/0000-0001-7164-1508
Rob Fender https://orcid.org/0000-0002-5654-2744
Paolo Goldoni https://orcid.org/0000-0001-5638-5817
Jeroen Homan https://orcid.org/0000-0001-8371-2713
Nicola Masetti https://orcid.org/0000-0001-9487-7740
Sara Motta https://orcid.org/0000-0002-6154-5843
Teo Muñoz-Darias https://orcid.org/0000-0002-3348-4035
Alessandro Papitto https://orcid.org/0000-0001-6289-7413
Thomas D. Russell https://orcid.org/0000-0002-7930-2276
Gregory Sivakoff https://orcid.org/0000-0001-6682-916X
Jakob van den Eijnden https://orcid.org/0000-0002-5686-0611

References

Albayati, A. C., Altamirano, D., Jaisawal, G. K., et al. 2021, MNRAS, 501, 261
Appenzeller, I., Fricke, K., Fürtig, W., et al. 1998, Msngr, 94, 1
Armas Padilla, M., Degenaar, N., Russell, D. M., & Wijnands, R. 2013, MNRAS, 428, 3083
Astropy Collaboration, Price-Whelan, A. M., Lim, P. L., et al. 2022, ApJ, 935, 167
Augusteijn, T., Kuulkers, E., & Shaham, J. 1993, A&A, 279, L13
Baglio, M. C., Russell, D. M., Crespi, S., et al. 2020, ApJ, 905, 87
Baglio, M. C., Saikia, P., Russell, D. M., et al. 2022, ApJ, 930, 20
Bernardini, F., Russell, D. M., Shaw, A. W., et al. 2016, ApJL, 818, L5
Blandford, R. D., & Königl, A. 1979, ApJ, 232, 34
Bramich, D. M., & Freudling, W. 2012, MNRAS, 424, 1584
Bright, J. S., Fender, R. P., Motta, S. E., et al. 2020, NatAs, 4, 697
Brocksopp, C., Jonker, P. G., Fender, R. P., et al. 2001, MNRAS, 323, 517
Burrows, D. N., Hill, J. E., Nousek, J. A., et al. 2005, SSRv, 120, 165
Buxton, M. M., & Bailyn, C. D. 2004, ApJ, 615, 880
Cardelli, J. A., Clayton, G. C., & Mathis, J. S. 1989, ApJ, 345, 245
Carotenuto, F., Corbel, S., Tremou, E., et al. 2021, MNRAS, 504, 444
CASA Team, Bean, B., Bhatnagar, S., et al. 2022, PASP, 134, 114501
Chandrasekhar, S. 1960, Radiative Transfer (Garden City, NY: Dover Publications)
Chen, W., Livio, M., & Gehrels, N. 1993, ApJL, 408, L5
Chen, W., Shrader, C. R., & Livio, M. 1997, ApJ, 491, 312
Condon, J. J. 1997, PASP, 109, 166
Condon, J. J., Cotton, W. D., Greisen, E. W., et al. 1998, AJ, 115, 1693
Corbel, S., & Fender, R. P. 2002, ApJL, 573, L35
Cúneo, V. A., Alabarta, K., Zhang, L., et al. 2020, MNRAS, 496, 1001
Cunningham, C. 1976, ApJ, 208, 534
Curran, P. A., Coriat, M., Miller-Jones, J. C. A., et al. 2014, MNRAS, 437, 3265
Curran, P. A., Miller-Jones, J. C. A., Rushton, A. P., et al. 2015, MNRAS, 451, 3975
Degenaar, N., Maitra, D., Cackett, E. M., et al. 2014, ApJ, 784, 122
Díaz Trigo, M., Altamirano, D., Dinçer, T., et al. 2018, A&A, 616, A23
Dubus, G., Hameury, J. M., & Lasota, J. P. 2001, A&A, 373, 251
Evans, P. A., Beardmore, A. P., Page, K. L., et al. 2007, A&A, 469, 379
Evans, P. A., Beardmore, A. P., Page, K. L., et al. 2009, MNRAS, 397, 1177
Falcke, H., Körding, E., & Markoff, S. 2004, A&A, 414, 895
Fender, R., & Gallo, E. 2014, SSRv, 183, 323
Fender, R., & Muñoz-Darias, T. 2016, in Lecture Notes in Physics, ed. F. Haardt et al., Vol. 905 (Berlin: Springer), 65
Fender, R., Woudt, P. A., Corbel, S., et al. 2016, in MeerKAT Science: On the Pathway to the SKA, 13
Fender, R. P., Belloni, T. M., & Gallo, E. 2004, MNRAS, 355, 1105
Fender, R. P., Hjellming, R. M., Tilanus, R. P. J., et al. 2001, MNRAS, 322, L23
Fender, R. P., Homan, J., & Belloni, T. M. 2009, MNRAS, 396, 1370
Fender, R. P., & Kuulkers, E. 2001, MNRAS, 324, 923
Fijma, S., van den Eijnden, J., Degenaar, N., Russell, T. D., & Miller-Jones, J. C. A. 2023, MNRAS, 521, 4490
Foight, D. R., Güver, T., Özel, F., & Slane, P. O. 2016, ApJ, 826, 66
Fomalont, E. B., Geldzahler, B. J., & Bradshaw, C. F. 2001, ApJ, 558, 283
Foreman-Mackey, D., Hogg, D. W., Lang, D., & Goodman, J. 2013, PASP, 125, 306
Fossati, L., Bagnulo, S., Mason, E., & Landi Degl’Innocenti, E. 2007, in ASP Conf. Ser. 364, The Future of Photometric, Spectrophotometric and Polarimetric Standardization, ed. C. Sterken (Cambridge: Cambridge Univ. Press), 503
Frank, J., King, A., & Raine, D. J. 2002, Accretion Power in Astrophysics: Third Edition (Cambridge: Cambridge Univ. Press)
Gallo, E., Degenaar, N., & van den Eijnden, J. 2018, MNRAS, 478, L132
Gallo, E., Miller, B. P., & Fender, R. 2012, MNRAS, 423, 590
Gandhi, P., Blain, A. W., Russell, D. M., et al. 2011, ApJL, 740, L13
Gao, F., & Han, L. 2012, Comput. Optim. Appl., 51, 259
Gasealahwe, K. V. S., Monageng, I. M., Fender, R. P., et al. 2024, MNRAS, 533, 1800
Gendreau, K. C., Arzoumanian, Z., Adkins, P. W., et al. 2020, Proc. SPIE,
Goodwin, A. J., Russell, D. M., Galloway, D. K., et al. 2020, MNRAS, 498, 3429
Gusinskaia, N. V., Hessels, J. W. T., Degenaar, N., et al. 2020, MNRAS, 492, 2858
Hameury, J. M. 2020, AdSpR, 66, 1004
Hameury, J. M., Lasota, J. P., McClintock, J. E., & Narayan, R. 1997, ApJ, 489, 234
Han, X., & Hjellming, R. M. 1992, ApJ, 400, 304
Harris, C. R., Millman, K. J., van der Walt, S. J., et al. 2020, Natur, 585, 357
Hartman, J. M., Galloway, D. K., & Chakrabarty, D. 2011, ApJ, 726, 26
Hasinger, G., & van der Klis, M. 1989, A&A, 225, 79
Heywood, I. 2020, oxkat: Semi-automated imaging of MeerKAT observations, Astrophysics Source Code Library, ascl:2009.003
Heywood, I., Jarvis, M. J., Hale, C. L., et al. 2022, MNRAS, 509, 2150
Hjellming, R. M., & Rupen, M. P. 1995, Natur, 375, 464
Hjellming, R. M., Stewart, R. T., White, G. L., et al. 1990, ApJ, 365, 681
Hogg, D. W., & Foreman-Mackey, D. 2018, ApJS, 236, 11
Homan, J., Buxton, M., Markoff, S., et al. 2005, ApJ, 624, 295
Homan, J., Neilsen, J., Allen, J. L., et al. 2016, ApJL, 830, L5
Hunter, J. D. 2007, CSE, 9, 90
Hynes, R. I. 2005, ApJ, 623, 1026
Illiano, G., Papitto, A., Ambrosino, F., Zanon, A. M., & Sanna, A. 2023, ATeL, 16125, 1
Jiménez-Ibarra, F., Muñoz-Darias, T., Armas Padilla, M., et al. 2019, MNRAS, 484, 2078
John, C., De, K., Lucchini, M., et al. 2024, MNRAS, 535, 2633
Jonas, J. & Team MeerKAT 2016, in MeerKAT Science: On the Pathway to the SKA (Trieste: SISSA)
Kalemci, E., Dinçer, T., Tomsick, J. A., et al. 2013, ApJ, 779, 95
King, A. R., & Ritter, H. 1998, MNRAS, 293, L42
Koljonen, K. I. I., Russell, D. M., Corral-Santana, J. M., et al. 2016, MNRAS, 460, 942
Lasota, J.-P. 2001, NewAR, 45, 449
Lewis, F., Russell, D. M., Fender, R. P., Roche, P., & Clark, J. S. 2008, arXiv:0811.2336
Lewis, F., Russell, D. M., Jonker, P. G., et al. 2010, A&A, 517, A72
Livio, M., & Pringle, J. E. 1992, MNRAS, 259, 23P
Lucy, L. B. 2016, A&A, 588, A19
Maitra, D., & Bailyn, C. D. 2008, ApJ, 688, 537
Menou, K., Hameury, J.-M., & Stehle, R. 1999, MNRAS, 305, 79
Meyer, F., & Meyer-Hofmeister, E. 1994, A&A, 288, 175
Migliari, S., & Fender, R. P. 2006, MNRAS, 366, 79
Migliari, S., Fender, R. P., Rupen, M., et al. 2004, MNRAS, 351, 186
Patruno, A., Maitra, D., Curran, P. A., et al. 2016, ApJ, 817, 100
Penninx, W., Lewin, W. H. G., Zijlstra, A. A., Mitsuda, K., & van Paradijs, J. 1988, Natur, 336, 146
Rhodes, L., Russell, D. M., Saikia, P., et al. 2024, MNRAS, 536, 3421
Roming, P. W. A., Kennedy, T. E., Mason, K. O., et al. 2005, SSRv, 120, 95
Rout, S. K., Muñoz-Darias, T., Homan, J., et al. 2025, ApJ, 978, 12
Rout, S. K., Vadawale, S. V., Aarthy, E., et al. 2021, JApA, 42, 39
Russell, D. M. 2018, Galax, 6, 3
Russell, D. M., Bramich, D. M., Lewis, F., et al. 2019, AN, 340, 278
Russell, T. D., Degenaar, N., van den Eijnden, J., et al. 2021, MNRAS, 508, L6

Russell, D. M., Fender, R. P., Hynes, R. I., et al. 2006, MNRAS, 371, 1334

Russell, D. M., Fender, R. P., & Jonker, P. G. 2007, MNRAS, 379, 1108

Russell, D. M., Lewis, F., Roche, P., et al. 2010, MNRAS, 402, 2671

Russell, D. M., Maitra, D., Dunn, R. J. H., & Fender, R. P. 2011, MNRAS, 416, 2311

Russell, D. M., Markoff, S., Casella, P., et al. 2013a, MNRAS, 429, 815

Russell, D. M., Qasim, A. A., Bernardini, F., et al. 2018, ApJ, 852, 90

Russell, D. M., Russell, T. D., Miller-Jones, J. C. A., et al. 2013b, ApJL, 768, L35

Russell, T. D., Soria, R., Miller-Jones, J. C. A., et al. 2014, MNRAS, 439, 1390

Rybicki, G. B., & Lightman, A. P. 1979, Radiative Processes in Astrophysics (Weinheim: John Wiley & Sons)

Saikia, P., Homan, J., Alabarta, K., et al. 2023a, ATeL, 16185, 1

Saikia, P., Russell, D. M., Alabarta, K., et al. 2023b, ATeL, 16119, 1

Saikia, P., Russell, D. M., Pirbhoy, S. F., et al. 2023c, ApJ, 949, 104

Shahbaz, T., Russell, D. M., Covino, S., et al. 2016, MNRAS, 463, 1822

Shakura, N. I., & Sunyaev, R. A. 1973, A&A, 500, 33

Sharma, S. 2017, ARA&A, 55, 213

Shidatsu, M., Tachibana, Y., Yoshii, T., et al. 2017, ApJ, 850, 155

Skrutskie, M. F., Cutri, R. M., Stiening, R., et al. 2006, AJ, 131, 1163

Smak, J. 1971, AcA, 21, 15

Smak, J. 1984, PASP, 96, 5

Spencer, R. E., Rushton, A. P., Bałucińska-Church, M., et al. 2013, MNRAS, 435, L48

Stetson, P. B. 1987, PASP, 99, 191

Stetson, P. B. 1990, PASP, 102, 932

Sunyaev, R. A., & Titarchuk, L. G. 1985, A&A, 143, 3 74

Tan, J., Lewin, W. H. G., Hjellming, R. M., et al. 1992, ApJ, 385, 314

Tetarenko, A. J., Sivakoff, G. R., Miller-Jones, J. C. A., et al. 2017, MNRAS, 469, 3141

Tonry, J. L., Denneau, L., Flewelling, H., et al. 2018, ApJ, 867, 105

Tudor, V., Miller-Jones, J. C. A., Patruno, A., et al. 2017, MNRAS, 470, 324

Tudose, V., Fender, R. P., Linares, M., Maitra, D., & van der Klis, M. 2009, MNRAS, 400, 2111

van den Eijnden, J., Degenaar, N., Russell, T. D., et al. 2021, MNRAS, 507, 3899

van Paradijs, J. 1996, ApJL, 464, L139

van Paradijs, J., & McClintock, J. E. 1994, A&A, 290, 1 33

van Paradijs, J., & Verbunt, F. 1984, in AIP Conf. Ser. 115, High Energy Transients in AstroPhysics, ed. S. E. Woosley (Melville, NY: AIP), 49

Veledina, A., Poutanen, J., & Vurm, I. 2013, MNRAS, 430, 3196

Virtanen, P., Gommers, R., Oliphant, T. E., et al. 2020, NatMe, 17, 261

Zhang, G. B., Bernardini, F., Russell, D. M., et al. 2019, ApJ, 876, 5

Zurita, C., Torres, M. A. P., Steeghs, D., et al. 2006, ApJ, 644, 432